DTU Library

Balanced nitrogen and hydrogen chemisorption by [RuH_6] catalytic center favors low-temperature NH_3 synthesis

Pan, Jaysree; Wang, Qianru; Guo, Jianping; Hansen, Heine Anton; Chen, Ping; Vegge, Tejs

Published in:
Cell Reports Physical Science

Link to article, DOI:
10.1016/j.xcrp.2022.100970

Publication date:
2022

Document Version
Publisher's PDF, also known as Version of record

Cell Reports Physical Science

CellPress OPEN ACCESS

Article

Balanced nitrogen and hydrogen chemisorption by [RuH_6] catalytic center favors low-temperature NH_3 synthesis

Jaysree Pan,[1,5] Qianru Wang,[2,3,5] Jianping Guo,[2,3] Heine Anton Hansen,[1] Ping Chen,[2,3,4,*] and Tejs Vegge[1,6,*]

SUMMARY

Ammonia is a central vector in sustainable global growth, but the usage of fossil feedstocks and centralized Haber-Bosch synthesis conditions causes >1.4% of global anthropogenic CO_2 emissions. While nitrogenase enzymes convert atmospheric N_2 to ammonia at ambient conditions, even the most active manmade inorganic catalysts fail due to low activity and parasitic hydrogen evolution at low temperatures. Here, we show that the [RuH_6] catalytic center in ternary ruthenium complex hydrides (Li_4RuH_6) activates N_2 preferentially and avoids hydrogen over-saturation at low temperatures and near ambient pressure by delicately balancing H_2 chemisorption and N_2 activation. The active [RuH_6] catalytic center is capable of achieving high yield at low temperatures via a shift in the rate-determining reaction intermediates and transition states, where the reaction orders in hydrogen and ammonia change dramatically. Temperature-dependent atomic-scale understanding of this unique mechanism is obtained with synchronized experimental and density functional theory investigations.

INTRODUCTION

Ammonia is critical to our food-production ecosystem[1,2] and the single most produced polluting chemical (~170 million tons per year)[3–5] while also holding the potential to become one of the most promising carbon-free and low-cost long-term energy carriers.[6,7] The industrial Haber-Bosch (H-B) process employs a Fe-based catalyst and fossil-fuel-sourced H_2 and requires harsh operating conditions (typically 673–723 K and 100–300 bar). The large-scale and centralized H-B process accounts for nearly 2% of the world's consumption of fossil fuels[8] and, consequently, over 1.44% of global anthropogenic CO_2 emissions.[5] The development of small-scale processes that rely on renewable electricity as an energy source to sustainably produce the H_2 feedstock would thus be transformative in several ways. It would provide critical technological support toward the audacious goal of carbon-free growth and ensure the green transition. Two indispensable targets, where renewable energy penetration is arduous, would be reached simultaneously—food production and clean mobility.[4,9,10] A decentralized, low CAPEX NH_3 synthesis process targeted at emerging markets with significant future population growth needs would also support the core UN sustainability goals.

While direct electrochemical ammonia production represents the Holy Grail, the documented yields remain very far from any kind of commercialization.[11] The discovery of efficient heterogeneous or homogeneous catalysts that exhibit high activity

[1]Department of Energy Conversion and Storage, Technical University of Denmark, 2800 Kongens Lyngby, Denmark

[2]Dalian National Laboratory for Clean Energy, Dalian Institute of Chemical Physics, Chinese Academy of Sciences, Dalian 116023, China

[3]University of Chinese Academy of Sciences, Beijing 100049, China

[4]State Key Laboratory of Catalysis, Dalian 116023, China

[5]These authors contributed equally

[6]Lead contact

*Correspondence: pchen@dicp.ac.cn (P.C.), teve@dtu.dk (T.V.)

https://doi.org/10.1016/j.xcrp.2022.100970

under mild conditions would thus be a key enabler for the decentralized production of green ammonia. For industrial ammonia synthesis, it is widely recognized that Ru-based catalysts work better than Fe-based catalysts under milder reaction conditions.[12,13] However, the high activation energy for direct N_2 dissociation and the severe poisoning effect of hydrogen on conventional Ru metal catalyst renders efficient NH_3 synthesis under lower temperatures (<623 K) and lower pressures (<50 bar) unattainable.[14] Therefore, there have been many attempts to develop new catalysts to efficiently catalyze N_2+H_2 to NH_3 under mild conditions.[15–18] Recently discovered, a new class of ammonia catalysts—the ternary ruthenium complex hydrides[19]—was a breakthrough in this endeavor. The ternary ruthenium hydride's ability to efficiently synthesize NH_3 at $\leq$10 bar and $\leq$573 K conditions lies in the unique chemistry of the coordination complex and the alkali (alkaline earth) metal framework, facilitating a catalytic mechanism bridging homogeneous and heterogeneous concepts, which are clearly distinct from the Ru metal catalyst. For ternary Ru complex hydride catalysts, Ru is in an ionic state, and N_2 undergoes non-dissociative hydrogenolysis over the hydride(H^-)- and electron-rich [RuH_6] complex with the aid of the surrounding Li or Ba cations. The dynamic and synergistic engagement of all the components of the ternary hydrides creates a reaction path with a narrow energy span and leads to ammonia production with superior activities.

In this article, we present the reaction mechanism facilitating ternary ruthenium complex hydrides to successfully produce NH_3 at low temperature (448 K $\leq$ T $\leq$ 573 K) by selective N_2 activation and escaping H_2 over-saturation. This work shows the unique ability of the [RuH_6] catalytic center in the ternary ruthenium hydride to shift its rate-determining intermediate states and transition states of the N_2+H_2 to NH_3 reaction path in response to the lowering of the reaction temperature, which brings a significant change in reaction order of hydrogen and ammonia. This variation in the kinetics as a function of operating conditions (temperature, reactant partial pressures, etc.) is not a common phenomenon in catalysis but is observed in some cases.[20–24] Nonetheless, the mechanistic details behind it are seldom investigated, especially at an atomic level. Here, we achieve this via seamless integration of experimental and computational techniques to reveal the temperature-dependent catalytic process. In addition to the overall multi-step reaction mechanism of N_2+H_2 to NH_3 conversion on [RuH_6] catalytic center established in our previous publication,[19] we further identified unique features significantly different from any known catalysts in this field. Here, we show for the first time the effect and implication of balanced chemisorption of N_2 and H_2 and the temperature-sensitive reaction intermediate on the ammonia synthesis mechanism. Our finding discloses that an electron-rich active center with a comparable affinity toward N_2 and H_2 are critical for mild-condition ammonia catalysis. The thorough fundamental understanding developed in this study can be further used to design new low-temperature ammonia catalysts with better performance and has the potential to drive green-ammonia technology in a new direction.

RESULTS AND DISCUSSION

Chemisorption of N_2 and H_2 over [RuH_6] catalytic center

Figure 1 shows that the [RuH_6] catalytic center in Ru complex hydride catalysts Li_4RuH_6 not only outperforms the B_5 site of Ru metal catalysts under the same working conditions but also produces NH_3 at low temperatures. As discussed below, two inherent properties of the [RuH_6] catalytic center are critical toward the observed outstanding activity at low temperatures: (1) its selectivity for chemisorbing N_2 over H_2 and (2) a self-adjusting mechanism of avoiding hydrogen over-saturation sustaining the N_2-to-NH_3 conversion cycle.

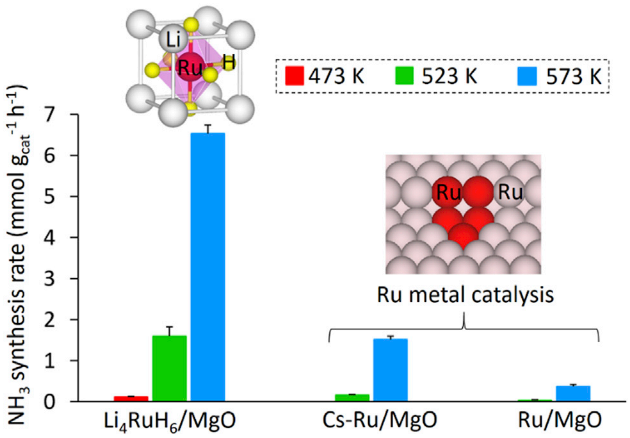

Figure 1. Comparison of NH_3 synthesis rate and active-site structure of ternary Ru complex hydride catalysts and Ru metal catalysts

[RuH_6] catalytic center is more efficient in NH_3 catalysis compared with metallic Ru and can produce NH_3 in low temperatures where metallic Ru gets deactivated. Reaction conditions: 1 bar of syngas (N_2:H_2 = 1:3), and a weight hourly space velocity (WHSV) of 60,000 mL g_{cat}^{-1} h^{-1}. Error bars represent the s.d. from three independent measurements.

The catalytically active ternary hydride surface with excess Li and hydrogen (consists of two additional LiH for every six [RuH_6] centers, i.e., 4[RuH_6]+2[RuH_7]+2Li)[19] is energetically moderately selective toward N_2 over H_2 chemisorption. The model considered the (110) plane of Li_4RuH_6, which is the most stable crystal facet for this material (Figure S1A). The details of the Li_4RuH_6 active surface used for this study are in Figure S1B. The presence of an additional two Li and two H (from two LiH) on the surface breaks its local symmetry. As a result, one of the [RuH_6] polyhedra turns into a pentagonal-based pyramid instead of a standard octahedron. This [RuH_6] site (denoted as [RuH_6]*) with a pentagonal-based pyramid is the preferred site for N_2/H_2 adsorption compared with other [RuH_6] sites with the octahedral coordination due to lower steric hindrance (Figure S1C). In contrast, [RuH_7] sites on the Li_4RuH_6 active surface cannot adsorb further any N_2/H_2. The extra two Li (from additional LiH) on the surface also create hindrances for N_2/H_2 adsorption on other neighboring [RuH_6] sites and cause partial deactivation. However, other [RuH_6]/[RuH_7] sites and the extra Li on the surface are vital for the N_2+H_2-to-NH_3 conversion process.[19] The [RuH_7]/[RuH_6] on the Li_4RuH_6 active surface was shown to act as a reservoir of hydrides to reduce the activated N_2 to NH_3, and the electrostatic interaction between surface Li and intermediate N_xH_y (x = 1–2, y = 0–4) species lowers the reaction path's thermodynamic/kinetic barrier, thus facilitating the N_2+H_2-to-NH_3 catalysis.[19]

The chemisorption H_2 on the Li_4RuH_6 active surface here can be expressed as

$$[RuH_6]^* + H_2 \leftrightarrow [RuH_6]H_2. \quad \text{(Equation 1)}$$

For simplicity, we are representing the Li_4RuH_6 active surface (which has four [RuH_6] complexes, two [RuH_7] complexes, and two extra Li) only by the active catalytic site [RuH_6]*. Here, the lattice hydrogens of Ru are inside the square brackets ([RuH_6]/[RuH_7]). The chemisorbed H_2 remains molecular ([RuH_6]H_2) until the H–H bond breaks (one of the hydrogens goes to the neighboring Ru ([RuH_6])) and becomes part of the lattice and creates two [RuH_7] in the process (see Figure S2). The transformation of the chemisorbed H_2 to lattice H can be written as

$$[RuH_6]H_2 + [RuH_6] \rightarrow 2[RuH_7]. \quad \text{(Equation 2)}$$

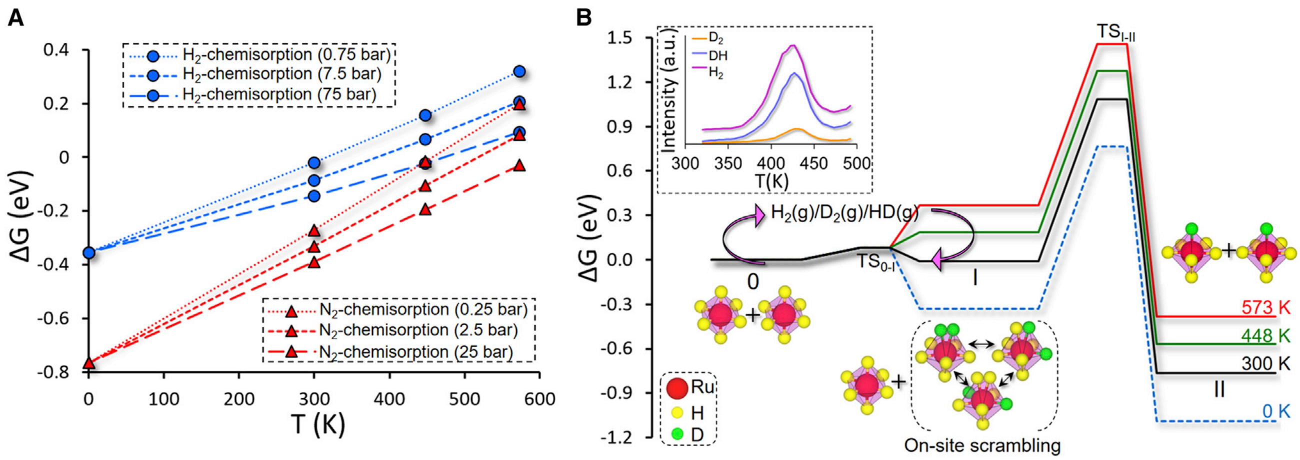

Figure 2. The mechanism to avoid hydrogen poisoning and activate N_2 in low temperature

(A) The competitive chemisorption of N_2 and H_2 by the $[RuH_6]$ center on the Li_4RuH_6 catalyst surface shows selectivity for N_2 over H_2, which improves at lower temperature[19] and remains selective over a wide range of partial pressures.

(B) The free-energy path of H_2/D_2 chemisorption/desorption along with on-site scrambling of the chemisorbed H_2/D_2 on the Li_4RuH_6 catalyst surface and a prohibitively high barrier (>1 eV) for chemisorbed H_2 to lattice H transfer demonstrates the mechanism by which $[RuH_6]$ catalytic center avoids hydrogen over-saturation. The top insertion shows the TPD profile of deuterated Li_4RuH_6.

Meanwhile, the competitive chemisorption of N_2 on the Li_4RuH_6 active surface is

$$[RuH_6]^* + N_2 \rightarrow [RuH_6]N_2. \qquad \text{(Equation 3)}$$

The calculated binding free energies show that the preferential adsorption of N_2 over H_2 at the $[RuH_6]$* active center is further enhanced at lower temperatures.[19] Figure 2A indicates that at low temperature, $[RuH_6]$* active center's inclination for selective chemisorption of N_2 might only change in the case of exceptionally high H_2:N_2 partial pressure ratio (~300:1). This feature is critical for the understanding of the catalytic mechanism, particularly when combined with the kinetics of dissociative hydrogen chemisorption and hydrogen transfer over the $[RuH_6]$ centers. Figure 2B displays the free-energy landscape for dissociation of chemisorbed H_2 (state I) on the $[RuH_6]$ active center (Equation 2). Although the dissociative chemisorption of H_2 into two lattice Hs is facile, the subsequent transfer of lattice H, as $[RuH_7]$ (state II), via a transition state (TS_{I-II}), is prohibited by a high activation energy of 1.1 eV (Figure S2), as estimated with nudged elastic band simulations. The transfer of the chemisorbed H_2 to lattice H is Li mediated and encounters repulsive force from neighboring Hs, making the activation barrier high. Instead, at low temperature, the active center retains the hydrogen atoms to form a $[RuH_6]H_2$ complex (state I), which is not a very stable state and can easily desorb H_2 at temperatures above 300 K to release the $[RuH_6]$ catalytic site for N_2 activation. The mechanism of H_2 chemisorption/desorption ensures that not all $[RuH_6]$ centers are converted to $[RuH_7]$ complexes, even in an H_2-rich environment. Thus, the catalyst surface is not hydrogen over-saturated by lattice H that bonds firmly to the respective Ru blocking the active sites. This contrasts with Ru and other late transition-metal catalysts, where H poisoning, due to favorable thermodynamics,[24] effectively prevents N_2 adsorption. The opposing behavior between Ru metal and Li_4RuH_6 catalysts is elegantly captured in the NH_3 formation rate under varying pressure (Figure 3). The lack of hydrogen poisoning allows enhanced ammonia production at a higher hydrogen partial pressure on Li_4RuH_6.

The chemisorption of H_2 on the ternary hydride active surface has unique fingerprints (Figure 2B). The chemisorption of H_2 happens through a physisorbed

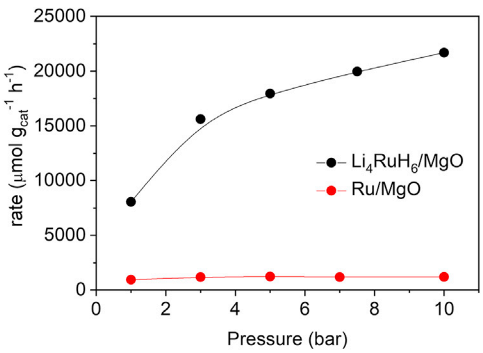

Figure 3. Pressure dependence of the catalytic activities of Li_4RuH_6/MgO and Ru/MgO catalysts at 573 K
The ability to avoid hydrogen oversaturation of [RuH_6] catalytic center enhances the NH_3 formation rate on Li_4RuH_6 catalyst in high hydrogen partial pressure. Reaction conditions: 10 bar, N_2:H_2 = 3:2, WHSV = 60,000 mL g_{cat}^{-1} h^{-1}.

transition state TS_{0-I}, with a negligible barrier of 0.07 eV (Figure S3). The H from the chemisorbed H_2 participates in on-site scrambling with the lattice H on the [RuH_6] active center. The on-site scrambling of the hydrogen has an insignificant activation energy of 0.04 eV (Figure S4). Experimentally, we observe a minor reversible adsorption/desorption of H_2 in the temperature range of 373–473 K in the temperature-programmed desorption (TPD) profile with no trace of net LiH, Ru powder, or a mixture of LiH and Ru (Figure S5), which reinforces the observation of the chemisorbed nature of the H_2 adsorption on the Li_4RuH_6 active surface. After charging with D_2, the detection of the mixed HD signal in the TPD profile strengthens the conclusion of the on-site scrambling of D from chemisorbed D_2 with lattice H (Figure 2B, inserted plot). A more robust signal of H_2/HD than D_2 in the TPD profile points out the magnitude of the on-site scrambling of the chemisorbed D_2 with the lattice H.

Low-temperature reaction mechanism

Our study shows that the N_2+H_2-to-NH_3 conversion cycle on the Li_4RuH_6 catalyst surface happens through 13 different surface states (states 0–12). Visualization of the low-temperature NH_3 formation mechanism on the Li_4RuH_6 catalyst surface with intermediate states is provided in Figure 4. Here, states 0 and 1 are the Li_4RuH_6 catalyst surface with active [RuH_6] center and the chemisorbed N_2 on it ([RuH_6]N_2), respectively, as presented by Equation (3). State 2 is ([RuH_5]NHN), where the adsorbed N_2 is hydrogenated by one of the hydrides from the same Ru site where N_2 is activated (i.e., H from [RuH_6]N_2):

$$[RuH_6]N_2 \rightarrow [RuH_5]NHN. \qquad \text{(Equation 4)}$$

State 3 is ([RuH_5]NHNH), in which the activated N_2 is further hydrogenated by one hydride from neighboring [RuH_7]:

$$[RuH_5]NHN + [RuH_7] \rightarrow [RuH_5]NHNH + [RuH_6]. \qquad \text{(Equation 5)}$$

In state 4 ([RuH_5]NHNH+2[RuH_7]), one H_2(g) gaseous molecule chemisorbs and then dissociates into two lattice hydrogens on the surface:

$$[RuH_5]NHNH + 2[RuH_6] + H_{2g} \rightarrow [RuH_5]NHNH + 2[RuH_7]. \qquad \text{(Equation 6)}$$

State 5 is ([RuH_5]$NHNH_2$), where the activated N_2 is further hydrogenated from one hydride of an adjacent [RuH_7] site:

$$[RuH_5]NHNH + [RuH_7] \rightarrow [RuH_5]NHNH_2 + [RuH_6]. \qquad \text{(Equation 7)}$$

The consecutive hydrogenations of the activated nitrogen weaken the N–N bond strength. The N–N bond length increases by about 30% (Figure 4) from state 1 to 5. Eventually, in state 6 ([RuH_5]NH+[RuH_6]NH_2), the N–N bond fully dissociates:

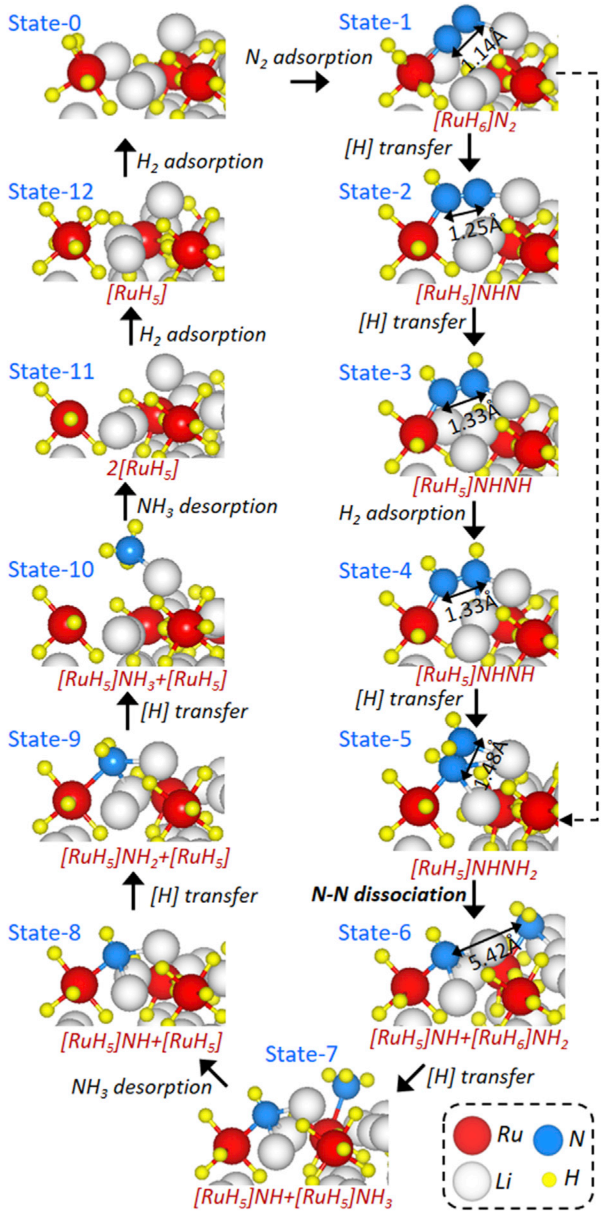

Figure 4. Visualization of the N_2-to-NH_3 conversion path on the Li_4RuH_6 catalyst surface
The catalytic conversion cycle went through 13 different surface states (marked by 0–12).[19] The hydrogenation of the activated nitrogen by the lattice hydrogen is marked as [H] transfer. The N–N bond distance increases with consecutive hydrogenation from steps 1 to 5 and eventually dissociates in state 6.

$$[RuH_5]NHNH_2 + [RuH_6] \rightarrow [RuH_5]NH + [RuH_6]NH_2. \quad \text{(Equation 8)}$$

In state 7 ($[RuH_5]NH+[RuH_5]NH_3$), the first molecule of NH_3 is formed, which then desorbs from the surface and creates state 8 ($[RuH_5]NH+[RuH_5]$):

$$[RuH_5]NH + [RuH_6]NH_2 \rightarrow [RuH_5]NH + [RuH_5]NH_3 \quad \text{(Equation 9)}$$

and

$$[RuH_5]NH + [RuH_5]NH_3 \rightarrow [RuH_5]NH + [RuH_5] + NH_{3g}. \quad \text{(Equation 10)}$$

In state 9 ($[RuH_5]NH_2+[RuH_5]$), the remaining N is hydrogenated further from the hydrides of an adjacent $[RuH_7]$ site:

$$[RuH_5]NH + [RuH_5] + [RuH_7] \rightarrow [RuH_5]NH_2 + [RuH_5] + [RuH_6]. \quad \text{(Equation 11)}$$

The 2nd molecule of NH_3 is formed in state 10 ($[RuH_5]NH_3+[RuH_5]$), which then desorbs from the surface and results in state 11 ($2[RuH_5]$):

$$[RuH_5]NH_2 + [RuH_5] + [RuH_7] \rightarrow [RuH_5]NH_3 + [RuH_5] + [RuH_6] \quad \text{(Equation 12)}$$

and

$$[RuH_5]NH_3 + [RuH_5] \rightarrow 2[RuH_5] + NH_{3g}. \quad \text{(Equation 13)}$$

Two consecutive direct adsorptions of H_2(g) molecule replenish the two hydride-deficient $[RuH_5]$ sites on the state 11, result in state 12 ($[RuH_5]$), and then finally return to state 0:

$$2[RuH_5] + H_{2g} \rightarrow [RuH_5] + [RuH_7] \quad \text{(Equation 14)}$$

and

$$[RuH_5] + H_{2g} \rightarrow \textit{renewed surface}. \quad \text{(Equation 15)}$$

The overall chemical reaction in one catalytic cycle on Li_4RuH_6 catalyst surface is

$$N_{2g} + 3H_{2g} \rightarrow NH_{3g}. \quad \text{(Equation 16)}$$

The path shows a series of well-balanced and moderate activation energies—all with $E_a \leq 0.82$ eV (see Table S1).

Temperature-dependent kinetics

For a better understanding of the low-temperature reaction pathway, the variations of reaction energetics as a function of temperature are explored and then analyzed by applying the energetic span model, in which the turnover frequency (TOF)-determining transition state (TDTS) and the TOF-determining intermediate state (TDI) that maximize the energy span determine the rates and kinetics of the catalytic cycle.[25,26] The energetic span approximation[25] of the exothermal catalytic cycle to calculate TOF from the energetic span (δE) of the free energy path is

$$TOF = \frac{k_B T}{h} e^{-\delta E / k_B T}. \quad \text{(Equation 17)}$$

In this model, the free energy of TDTS (ΔG_{TDTS}) and TDI (ΔG_{TDI}) and the free energy of reaction (ΔG_r) defines δE:

$$\delta E = \begin{cases} \Delta G_{TDTS} - \Delta G_{TDI}, & \text{if TDTS appears after TDI} \\ \Delta G_{TDTS} - \Delta G_{TDI} + \Delta G_r & \text{if TDTS appears before TDI} \end{cases} \quad \text{(Equation 18)}$$

The activation enthalpy (ΔH_a) for the catalytic path is back calculated from the δE and the entropy correction (TΔS):

$$\Delta H_a = \delta E + T\Delta S. \quad \text{(Equation 19)}$$

Figures 5 and S6 show the development of the free-energy path of the catalytic cycle of N_2+H_2 to NH_3 on the Li_4RuH_6 catalyst surface with a lowering of reaction temperature (from 573 to 448 K). The change in temperature shifts the TDI and TDTS of the catalytic cycle, with an inflection temperature at 498 K. Experimentally, the Arrhenius plot for ammonia synthesis (Figure 6A) locates this inflection point around 523 K. In addition, all measured kinetic parameters for ternary hydride catalyst (Li_4RuH_6/MgO) are temperature dependent (Figure 6), indicating the complex temperature-dependent switching of rate-determining states (i.e., TDI and TDTS).

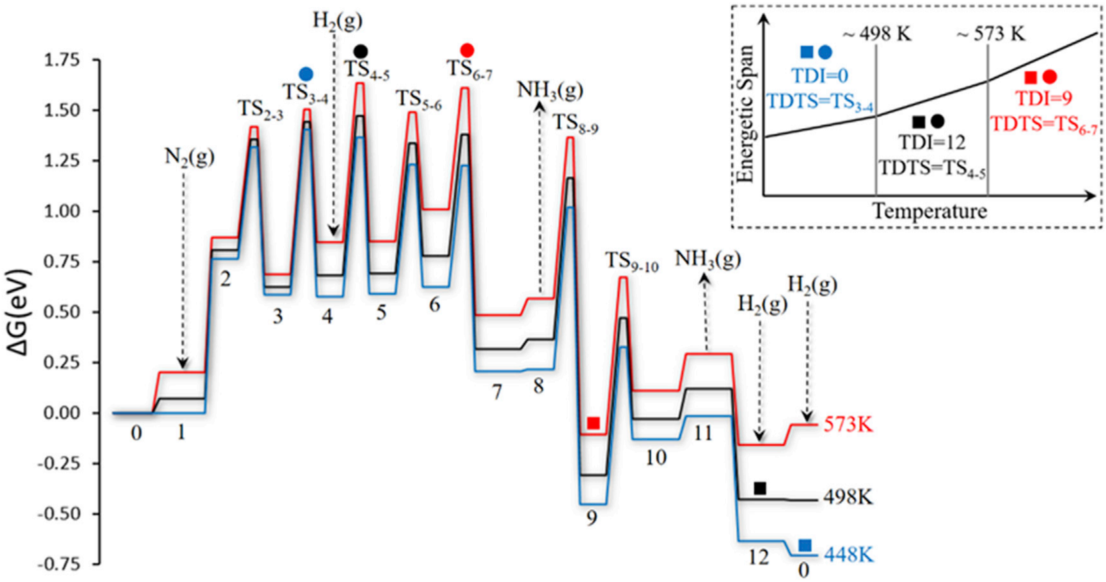

Figure 5. Temperature dependence

The evolution of the free-energy path with the lowering of temperature shifts the TDI and the TDTS of the energetic span model, and the inflection point is at 498 K of Li_4RuH_6 catalyst surface. For the lower temperature range (<498 K), the TDI and TDTS are the initial/final state (state 0) and the transition state of the third hydrogenation ($TS_{3–4}$) on the surface, respectively. In the higher temperature range (≥498 K), the TDI and the TDTS are the second H_2(g) adsorption (state 12) and the transition state of the first H_2(g) adsorption ($TS_{4–5}$) on the surface, respectively. With a further increase in temperature, state 9 comes energetically closer to state 12. At 573 K, the TDI and the TDTS are state 9 and $TS_{4–5}$, respectively. The inserted plot shows the schematic presentation of the shift in TDI/TDTS. The TDI and TDTS at different temperature ranges are marked by the square and circlesymbols, respectively, in the free-energy plot and the inserted plot. We applied fixed partial pressure of N_2 and H_2 (P_{N2} = 0.25 bar and P_{H2} = 0.75 bar) and variable partial pressure of ammonia (P_{NH3} = 0.0270 bar at 573K, 0.0018 bar at 498 K, and 0.0001 bar at 448 K) to generate the free-energy paths and barriers using density-functional-theory-based free-energy estimations and nudged elastic band method.

As shown in Figure 5, the TDTS moves from the transition states 4–5 ($TS_{4–5}$) to $TS_{3–4}$ as the temperature goes lower than the inflection point 498 K. Meanwhile, the TDI shifts from state 12 to 0. For clarity, the inserted plot in Figure 5 presents a schematic view of the shift in TDI/TDTS with temperature. There might be one inflection for each change in TDI/TDTS, which we cannot resolve due to their proximity. Another essential feature in the catalytic path is the energy difference between states 12 and 9. At 573 K, the free energies of states 9 and 12 are similar, and they are both likely candidates for the TDI. The energy difference between states 12 and 9 increases with decreasing temperature, and state 12 is TDI in the range 498 K < T < 573 K. The theoretically derived activation enthalpy (ΔH_a) and TOF and experimentally derived apparent activation energy (E_{app}) and TOF are listed in Table S2. The value of ΔH_a at 448 K is 98.2 kJ mol^{-1}, while at 573 K, with state 9 as TDI, the ΔH_a is calculated to be 72.4 kJ mol^{-1}. An increase in temperature lowers the activation enthalpy and increases the TOF, agreeing well with the trends observed experimentally. The apparent activation energy for Li_4RuH_6 catalyst determined by Arrhenius plot is E_{app} = 71.2 kJ/mol at temperatures higher than 523 K and a significantly increased value of 102.8 kJ/mol at temperatures below 523 K (Figure 6A). In contrast, there is no change in E_{app} and other kinetic parameters for conventional Ru metal catalyst (Ru/MgO) in a wide temperature range (498–648 K).

For the Li_4RuH_6 catalyst, the energetic span and the TOF vary continuously with temperature. The temperature-dependent TDI and TDTS modifications follow the entropy of intermediates and TSs. The entropy of a state is strongly affected by the adsorption/desorption of gas molecules. Such changes in the TDI or TDTS will

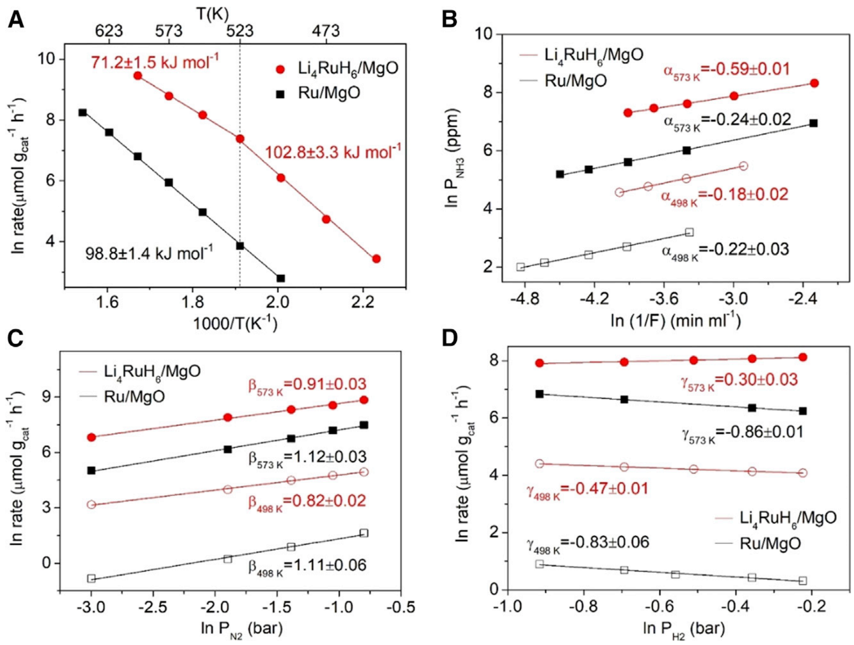

Figure 6. Experimentally derived kinetic parameters

(A) Arrhenius plots of supported Li_4RuH_6/MgO and Ru/MgO catalysts.

(B–D) Dependence of ammonia synthesis rates on the partial pressures of NH_3 (B), N_2 (C), and H_2 (D), respectively, under a total pressure of 1 bar at 573 (filled symbols) and 498 K (open symbols) over supported Li_4RuH_6/MgO and Ru/MgO catalysts. The reaction order of NH_3, N_2, and H_2 is represented by α, β, and γ, respectively. In contrast to metallic Ru, *[RuH6]* catalytic center shows changes in NH_3 TOF and reactions order of N_2, H_2, and NH_3 on lowering of temperature.

tend to affect both ΔH_a and the reaction order in gas molecules. This is beautifully captured by the analysis of the reaction order of NH_3, N_2, and H_2 for Li_4RuH_6 (Figures 6B–6D). The reaction orders changed from +0.3 to −0.47, 0.91 to 0.82, and −0.59 to −0.18, respectively, for H_2, N_2, and NH_3 with the decrease of temperature. These changes are in stark contrast to the constant values for Ru metal catalyst (Ru/MgO), i.e., −0.23, 1.12, and −0.85, respectively for H_2, N_2, and NH_3. It is worth noting that although the H_2 reaction orders of ternary Ru hydride catalysts decrease with the decrease of temperature, they are still higher than that of the Ru metal catalyst. Moreover, NH_3 poisoning effects on the [RuH_6] center lessens at lower temperatures, providing a favorable scenario for effective catalysis.

The present study highlights the dynamic nature of the [RuH_6] catalytic center in enabling mild condition ammonia synthesis. The presence of [RuH_7] complex facilitates the hydrogenation of the activated nitrogen from the surplus lattice hydrides. On the contrary, a too-high concentration of [RuH_7] complex on the surface can deactivate the catalyst from dinitrogen adsorption. The high activation energy for lattice H transfer of the chemisorbed H_2 observed in this unique class of materials maintains a delicate balance between the availability of lattice hydrogen and active sites. The preferential N_2 chemisorption over H_2 and kinetic blockage of hydrogen over-saturation are key elements to the success of ternary Ru complex hydride systems for catalyzing NH_3 synthesis at low temperatures. Furthermore, a unique temperature-dependent tuning of the reaction kinetics is observed for the [RuH_6] catalytic center, resulting from a shift in the TDI and TDTS along the reaction pathway.

We have been able to achieve a precise temperature-resolved atomic-scale understanding of the reaction mechanism at the [RuH_6] catalytic center, its unique thermodynamics, and kinetic aspects that enable exceptional low-temperature activity. These scientific insights need to be exploited toward optimizing complex transition-metal hydrides as ammonia catalysts as well as exploring a newer class of materials that can replicate the behavior of [RuH_6] catalytic center in the pursuit of renewables-powered, decentralized, and ambient-temperature/pressure ammonia synthesis.

EXPERIMENTAL PROCEDURES

Resource availability

Lead contact

Further information and requests for resources should be directed to and will be fulfilled by the lead contact, Tejs Vegge (teve@dtu.dk).

Materials availability

This study did not generate new unique materials.

Data and code availability

All data supporting the findings of this study are presented within the article and supplemental information. Optimized structures are available in an online repository (https://doi.org/10.11583/DTU.16621918.v1). All other data are available from the lead contact upon reasonable request.

Materials

The materials used were as follows: LiH (Alfa, 99.4% metal basis); Ru powder (Aladdin, 99.9% metal basis); $Ru(NO)(NO_3)_2$ (Alfa, Ru $\geq$31.3%); $CO(NH_2)_2$ (SCR, $\geq$99%); $Mg(CH_3COO)_2 \cdot 4H_2O$ (SCR, $\geq$99%); $C_2H_2O_4 \cdot 2H_2O$ (SCR, $\geq$99.5%), Ba metal (Aldrich, $\geq$99% trace metals basis, shot diameter: $\sim$2 cm); Li metal (Macklin, 99.9% metal basis), and $CsNO_3$ (Guangfu, $\geq$99%). All materials handlings were performed in a glove box filled with purified argon to keep a low water vapor concentration (<0.1 ppm) and a low oxygen concentration (<1 ppm). H_2 (99.9999%), D_2 (99.999%), Ar (99.999%), and N_2/H_2 mixture with a molar ratio of 1:3 (99.9999%) were purchased from Dalian Special Gases.

Preparation of ball-milled LiH, ball-milled Ru powder, and ball-milled LiH-Ru mixture

Ball-milled LiH was prepared by ball milling LiH on a Retsch planetary ball mill (PM 400, Germany) at 150 RPM for 3 h. Ru powder was also ball-milled at 150 RPM for 3 h and then heated at 753 K for 10 h under 10 bar of H_2, and the obtained sample was denoted as ball-milled Ru powder. The ball-milled LiH-Ru mixture was prepared by ball milling a mixture of LiH and Ru powder in a 4:1 M ratio at 150 RPM for 3 h.

Preparation of fresh Li_4RuH_6, post-treated Li_4RuH_6, and deuterated Li_4RuH_6 samples

A fresh Li_4RuH_6 sample was synthesized by the calcination of ball-milled LiH-Ru mixture under 10 bar of H_2 at 753 K for 10 h, as has been described in earlier reports.[27,28] The post-treated Li_4RuH_6 sample was prepared as follows. The fresh Li_4RuH_6 was first dehydrogenated under atmospheric Ar up to 493 K and then rehydrogenated under atmospheric H_2 at 393 K for 2 h. At last, the obtained sample was cooled to room temperature for use. The deuterated Li_4RuH_6 sample was prepared in a similar way, except rehydrogenating the dehydrogenated Li_4RuH_6 under atmospheric D_2.

Preparation of Ru/MgO, Cs-Ru/MgO, and Li_4RuH_6/MgO catalysts

Ru/MgO and Cs-Ru/MgO reference catalysts with Ru content of 8.7 and 7.3 wt %, respectively, were prepared following the procedure described in the earlier report.[19] Li_4RuH_6/MgO catalyst with a Ru loading of 8.0 wt % was prepared according to the following steps: firstly, the Ru/MgO sample was impregnated in a lithium-ammonia solution with a molar ratio of Li:Ru = 4:1, where Li metal can be easily converted to lithium amide ($LiNH_2$) in the presence of Ru. After removal of excess NH_3, the solid residue was then hydrogenated at 573 K to allow *in situ* formation of Li_4RuH_6 on MgO support according to the reaction $4LiNH_2 + Ru + 5H_2 \rightarrow Li_4RuH_6 + 4NH_3$.

Catalytic activity test

Activity test was performed on a quartz-lined stainless-steel fix-bed reactor under a continuous flow of N_2-H_2 mixture gas. Typically, 30 mg of catalyst was loaded in the liner tube on a bed of quartz wool and subsequently heated at a ramping rate of 5 K min^{-1} under the given pressure and flow rate. The ammonia production rate was measured by a conductivity meter (Mettler Toledo SevenMulti), and the principle of this NH_3 quantification method has been described previously.[29] The activity data at each temperature were monitored under steady-state conditions.

TPD measurements

TPD measurements were performed on a stainless-steel reactor with a quartz liner, and the exhaust gases were monitored with an on-line mass spectrometer (Hiden HPR20). Typically, a 30 mg sample was loaded and heated in a stream of Ar (30 mL min^{-1}) from room temperature to the desired temperature at a ramping rate of 5 K min^{-1}, and the signals of H_2 (m/z = 2), HD (m/z = 3), and D_2 (m/z = 4) were recorded.

Kinetic studies

N_2 and H_2 reaction order measurements were carried out with a flow of mixed gas (N_2, H_2, and Ar) under a total pressure of 1 bar and a weight hourly space velocity (WHSV) of 60,000 mL g^{-1} h^{-1}, during which the effluent NH_3 concentration was kept constant. For Li_4RuH_6/MgO, the loading amount was 30 mg at both 573 and 498 K. For Ru/MgO, the loading amount was 50 mg at 573 K and 100 mg at 498 K, respectively. The reaction order of N_2 was determined through changing the partial pressure of N_2 while keeping a constant partial pressure of H_2, and the reaction order of H_2 was measured at a constant N_2 pressure while changing the partial pressure of H_2. The reaction order of NH_3 was determined by changing the flow rate of syngas (N_2:H_2 = 1:3) while keeping constant pressure. Apparent activation energies were measured under atmospheric syngas (N_2:H_2 = 1:3) with a flow rate of 30 mL min^{-1}. The temperature range is 448–598 K for Li_4RuH_6/MgO (30 mg) and 498–648 K for Ru/MgO (30 mg). All kinetic measurements were performed under conditions far from equilibrium.

Theoretical calculations

We used first-principles-based density functional theory (DFT) tool Vienna Ab initio simulation package (VASP)[30] to simulate the system. All calculations used a revised Perdew-Burke-Ernzerhof approximation (RPBE)[31] for the exchange-correlation potential, a plane-wave basis set with energy cutoff 500 eV, and the projector augmented wave (PAW) method. The DFT energies with the correction from ideal gas limit approximation[32,33] and harmonic limit/hindered harmonic limit approximation model implemented in atomistic simulation environment (ASE)[34] for the free molecules and the absorbates on the catalyst surface, respectively, generated the free energies reported in this work. The nudged elastic band method (NEB)[35] implemented in VASP was used to find the optimal kinetic paths, the TS, and the related activation energy. The four-layered Li_4RuH_6 slab used in this study has a (110) surface with six Ru sites on it. An 18 Å vacuum was used above the top layer of the slabs to prevent any interaction between two periodic images. We fixed the ions in the bottom two layers through the simulations.

SUPPLEMENTAL INFORMATION

Supplemental information can be found online at https://doi.org/10.1016/j.xcrp.2022.100970.

ACKNOWLEDGMENTS

J.P., H.A.H., and T.V. thank the Villum Foundations for financial support through the research center V-Sustain (#9455). T.V. also acknowledges support from the Independent Research Fund Denmark (DELIGHT#0217-00326B). Q.W., P.C., and J.G. are thankful for the financial support from National Key R&D Program of China (no. 2021YFB4000401), National Natural Science Foundation of China (grant nos. 21922205, 21988101, and 21872137), Youth Innovation Promotion Association CAS (no. 2018213), Liaoning Revitalization Talents Program (XLYC2007173 and XLYC2002076), and K.C. Wong Education Foundation (GJTD-2018-06).

AUTHOR CONTRIBUTIONS

J.P. did all the theoretical calculations and prepared the manuscript and the supplemental information. Q.W. did all the experiments and co-prepared the manuscript and the supplemental information. H.A.H. supervised the theoretical calculations, and J.G. supervised the experimental work. T.V. and P.C. conceived the project, supervised the research work, and acquired the funding for it. All authors participated in the discussion, data analysis, and finalizing of the manuscript.

DECLARATION OF INTERESTS

The authors declare no competing financial interest.

Received: March 16, 2022
Revised: May 10, 2022
Accepted: June 9, 2022
Published: July 20, 2022

REFERENCES

1. Smil, V. (1999). Detonator of the population explosion. Nature *400*, 415. https://doi.org/10.1038/22672.

2. Erisman, J.W., Sutton, M.A., Galloway, J., Klimont, Z., and Winiwarter, W. (2008). How a century of ammonia synthesis changed the world. Nat. Geosci. *1*, 636–639. https://doi.org/10.1038/ngeo325.

3. Brunning, A. (2019). Periodic Graphics: environmental impact of industrial reactions. Chem. Eng. News *97*, 23. https://cen.acs.org/energy/Periodic-Graphics-Environmental-impact-industrial/97/i24.

4. Pfromm, P.H. (2017). Towards sustainable agriculture: fossil-free ammonia. J. Renew. Sustain. Energy *9*, 034702. https://doi.org/10.1063/1.4985090.

5. Soloveichik, G. (2019). Electrochemical synthesis of ammonia as a potential alternative to the Haber–Bosch process. Nat. Catal. *2*, 377–380. https://doi.org/10.1038/s41929-019-0280-0.

6. Valera-Medina, A., Xiao, H., Owen-Jones, M., David, W.I.F., Bowen, P.J., and VAlerA-MedinA, A. (2018). Ammonia for power. Prog. Energy Combust. Sci. *69*, 63–102. https://doi.org/10.1016/j.pecs.2018.07.001.

7. Klerke, A., Christensen, C.H., Nørskov, J.K., and Vegge, T. (2008). Ammonia for hydrogen storage: challenges and opportunities. J. Mater. Chem. *18*, 2304–2310. https://doi.org/10.1039/b720020j.

8. Wang, Q., Guo, J., and Chen, P. (2019). Recent progress towards mild-condition ammonia synthesis. J. Energy Chem. *36*, 25–36. https://doi.org/10.1016/j.jechem.2019.01.027.

9. Giddey, S., Badwal, S.P.S., Munnings, C., and Dolan, M. (2017). Ammonia as a renewable energy transportation media. ACS Sustain. Chem. Eng. *5*, 10231–10239. https://doi.org/10.1021/acssuschemeng.7b02219.

10. MacFarlane, D.R., Cherepanov, P.V., Choi, J., Suryanto, B.H.R., Hodgetts, R.Y., Bakker, J.M., Ferrero Vallana, F.M., Vallana, F.M.F., and Simonov, A.N. (2020). A roadmap to the ammonia economy. Joule *4*, 1186–1205. https://doi.org/10.1016/j.joule.2020.04.004.

11. Andersen, S.Z., Čolić, V., Yang, S., Schwalbe, J.A., Nielander, A.C., McEnaney, J.M., Enemark-Rasmussen, K., Baker, J.G., Singh, A.R., Rohr, B.A., et al. (2019). A rigorous

electrochemical ammonia synthesis protocol with quantitative isotope measurements. Nature *570*, 504–508. https://doi.org/10.1038/s41586-019-1260-x.

12. Aika, K.I. (2017). Role of alkali promoter in ammonia synthesis over ruthenium catalysts—effect on reaction mechanism. Catal. Today *286*, 14–20. https://doi.org/10.1016/j.cattod.2016.08.012.

13. Brown, D.E., Edmonds, T., Joyner, R.W., McCarroll, J.J., and Tennison, S.R. (2014). The genesis and development of the commercial BP doubly promoted catalyst for ammonia synthesis. Catal. Lett. *144*, 545–552. https://doi.org/10.1007/s10562-014-1226-4.

14. Vojvodic, A., Medford, A.J., Studt, F., Abild-Pedersen, F., Khan, T.S., Bligaard, T., and Nørskov, J. (2014). Exploring the limits: a low-pressure, low-temperature Haber–Bosch process. Chem. Phys. Lett. *598*, 108–112. https://doi.org/10.1016/j.cplett.2014.03.003.

15. Wang, P., Chang, F., Gao, W., Guo, J., Wu, G., He, T., and Chen, P. (2017). Breaking scaling relations to achieve low-temperature ammonia synthesis through LiH-mediated nitrogen transfer and hydrogenation. Nat. Chem. *9*, 64–70. https://doi.org/10.1038/nchem.2595.

16. Kitano, M., Inoue, Y., Yamazaki, Y., Hayashi, F., Kanbara, S., Matsuishi, S., Yokoyama, T., Kim, S.-W., Hara, M., and Hosono, H. (2012). Ammonia synthesis using a stable electride as an electron donor and reversible hydrogen store. Nat. Chem. *4*, 934–940. https://doi.org/10.1038/nchem.1476.

17. Gong, Y., Wu, J., Kitano, M., Wang, J., Ye, T.-N., Li, J., Kobayashi, Y., Kishida, K., Abe, H., Niwa, Y., et al. (2018). Ternary intermetallic LaCoSi as a catalyst for N2 activation. Nat. Catal. *1*, 178–185. https://doi.org/10.1038/s41929-017-0022-0.

18. Foster, S.L., Bakovic, S.I.P., Duda, R.D., Maheshwari, S., Milton, R.D., Minteer, S.D., Janik, M.J., Renner, J.N., and Greenlee, L.F. (2018). Catalysts for nitrogen reduction to ammonia. Nat. Catal. *1*, 490–500. https://doi.org/10.1038/s41929-018-0092-7.

19. Wang, Q., Pan, J., Guo, J., Hansen, H.A., Xie, H., Jiang, L., Hua, L., Li, H., Guan, Y., Wang, P., et al. (2021). Ternary ruthenium complex hydrides for ammonia synthesis via the associative mechanism. Nat. Catal. *4*, 959–967. https://doi.org/10.1038/s41929-021-00698-8.

20. Wang, Y.-G., Cantu, D.C., Lee, M.-S., Li, J., Glezakou, V.-A., and Rousseau, R. (2016). CO oxidation on Au/TiO2: condition-dependent active sites and mechanistic pathways. J. Am. Chem. Soc. *138*, 10467–10476. https://doi.org/10.1021/jacs.6b04187.

21. Xu, J., Deng, Y.-Q., Zhang, X.-M., Luo, Y., Mao, W., Yang, X.-J., Ouyang, L., Tian, P., and Han, Y.-F. (2014). Preparation, characterization, and kinetic study of a core–shell Mn3O4@SiO2 nanostructure catalyst for CO oxidation. ACS Catal. *4*, 4106–4115. https://doi.org/10.1021/cs5011376.

22. Fujita, T., Ishida, T., Shibamoto, K., Honma, T., Ohashi, H., Murayama, T., and Haruta, M. (2019). CO oxidation over Au/ZnO: unprecedented change of the reaction mechanism at low temperature caused by a different O2 activation process. ACS Catal. *9*, 8364–8372. https://doi.org/10.1021/acscatal.9b02128.

23. Noor, T., Qi, Y., and Chen, D. (2020). Hydrogen dependence of the reaction mechanism and kinetics of water gas shift reaction on Ni catalyst: experimental and DFT study. Appl. Catal. B Environ. *264*, 118430. https://doi.org/10.1016/j.apcatb.2019.118430.

24. Cortés, J., Valencia, E., Herrera, J., and Araya, P. (2007). Mechanism and kinetics parameters of the reduction reaction of NO by CO on Pd/Al2O3 catalyst. J. Phys. Chem. C *111*, 7063–7070. https://doi.org/10.1021/jp070697b.

25. Kozuch, S., and Shaik, S. (2011). How to conceptualize catalytic cycles? The energetic span model. Acc. Chem. Res. *44*, 101–110. https://doi.org/10.1021/ar1000956.

26. Kozuch, S. (2012). A refinement of everyday thinking: the energetic span model for kinetic assessment of catalytic cycles. WIREs Comput. Mol. Sci. *2*, 795–815. https://doi.org/10.1002/wcms.1100.

27. Sato, T., Takagi, S., Matsuo, M., Aoki, K., Deledda, S., Hauback, B.C., and Orimo, S.I. (2014). Raman and infrared spectroscopic studies on Li_4RuH_6 combined with first-principles calculations. Mater. Trans. *55*, 1117–1121. https://doi.org/10.2320/matertrans.mg201403.

28. Kritikos, M., and Noréus, D. (1991). Synthesis and characterization of ternary alkaline-earth transition-metal hydrides containing octahedral [Ru(II)H6]4− and [Os(II)H6]4− complexes. J. Solid State Chem. *93*, 256–262. https://doi.org/10.1016/0022-4596(91)90297-u.

29. Gao, W., Guo, J., Wang, P., Wang, Q., Chang, F., Pei, Q., Zhang, W., Liu, L., and Chen, P. (2018). Production of ammonia via a chemical looping process based on metal imides as nitrogen carriers. Nat. Energy *3*, 1067–1075. https://doi.org/10.1038/s41560-018-0268-z.

30. Kresse, G., and Joubert, D. (1999). From ultrasoft pseudopotentials to the projector augmented-wave method. Phys. Rev. B *59*, 1758–1775. https://doi.org/10.1103/physrevb.59.1758.

31. Hammer, B., Hansen, L.B., and Nørskov, J.K. (1999). Improved adsorption energetics within density-functional theory using revised Perdew-Burke-Ernzerhof functionals. Phys. Rev. B *59*, 7413–7421. https://doi.org/10.1103/physrevb.59.7413.

32. Sprowl, L.H., Campbell, C.T., and Árnadóttir, L. (2016). Hindered translator and hindered rotor models for adsorbates: partition functions and entropies. J. Phys. Chem. C *120*, 9719–9731. https://doi.org/10.1021/acs.jpcc.5b11616.

33. Cramer, C.J. (2013). Essentials of Computational Chemistry: Theories and Models (John Wiley & Sons).

34. Hjorth Larsen, A., Jørgen Mortensen, J., Blomqvist, J., Castelli, I.E., Christensen, R., Dułak, M., Friis, J., Groves, M.N., Hammer, B., Hargus, C., et al. (2017). The atomic simulation environment-A Python library for working with atoms. J. Phys. Condens. Matter *29*, 273002. https://doi.org/10.1088/1361-648x/aa680e.

35. Jónsson, H., Mills, G., and Jacobsen, K.W. (1998). Nudged elastic band method for finding minimum energy paths of transitions. In Classical and Quantum Dynamics in Condensed Phase Simulations (World Scientific), pp. 385–404.